View metadata, citation and similar papers at core.ac.uk
brought to you by CORE
provided by RERO DOC Digital Library

which should be cited to refer to this work.

Electron-hole fluctuation phase in 1*T*-$TiSe_2$

C. Monney,[1] G. Monney,[2] P. Aebi,[2,*] and H. Beck[2]
[1]*Research Department of Synchrotron Radiation and Nanotechnology, Paul Scherrer Institut, CH-5232 Villigen PSI, Switzerland*
[2]*Département de Physique and Fribourg Center for Nanomaterials, Université de Fribourg, CH-1700 Fribourg, Switzerland*

To address the fluctuation regime above the critical temperature of the charge-density-wave phase of 1*T*-$TiSe_2$, we perform calculations using the Bethe-Salpeter equation for treating strong electron-hole correlations. Calculated photoemission intensity maps are in good agreement with the measured ones and provide a deeper understanding of the phase transition in terms of an electronic instability. We find that no real nesting of the Fermi surface is necessary, but crossing points between different Fermi surface sheets produce an instability with a wave vector corresponding to the commensurate charge distribution observed below the critical temperature. Finally, we also consider the effect of the electron-phonon interaction on the calculated spectra to discriminate what mechanism is responsible for the instability and conclude that the electron-hole fluctuation scenario is more likely to occur.

http://doc.rero.ch

I. INTRODUCTION

Coulomb interaction plays a fundamental role in the behavior of condensed-matter systems. A particular effect is generated by the attractive Coulomb interaction between holes in the valence band and electrons in the conduction band of certain metals and semiconductors. It induces strong correlations between the two types of charge carriers. When the potential is weakly screened, and the gap between the bands is sufficiently small, it can build up bound states, called excitons. At low temperature these excitations can condense into a macroscopic state. This "excitonic insulator phase"[1] has been theoretically described in the 1960s. It was introduced for a system with valence and conduction bands of semimetallic or semiconducting configuration, the bands exhibiting extrema at the same location in reciprocal space.

The resulting superfluid is charge neutral, and thus difficult to evidence. Indeed, no experimental realization of the excitonic insulator phase has been unambiguously discovered yet, although potential candidates have been put forward.[2–6] Recently, more theoretical work on the possible realization of the excitonic insulator phase in particular systems has been presented.[7,8] 1*T*-$TiSe_2$ turns out to be a good candidate for the realization of such an excitonic insulator phase,[9,10] assuming a semimetallic band structure with a low carrier density in its normal phase.[11,12] The compound undergoes at about $T_c = 200$ K a second-order phase transition towards a charge-density-wave (CDW) phase,[13] with a $(2 \times 2 \times 2)$ superstructure of the lattice. The fact that it breaks the translational symmetry of the normal phase is a sign of a strong link between the lattice and the electronic band structure. Indeed, the extrema of the relevant valence and conduction bands sit at different locations in the Brillouin zone (BZ),[14] linked precisely by the wave vectors of the lattice deformation.

In previous work we have already interpreted the photoemission spectra in 1*T*-$TiSe_2$ below T_c by invoking the influence of the excitonic condensate on the electronic spectral functions.[15] Spectral features similar to those of the exciton condensate phase have also been observed above T_c.[15] This unusual regime has been attributed to the presence of strong electron-hole fluctuations anticipating the formation of the exciton condensate. Here, we study the fluctuation regime above the critical temperature T_c of the transition to the CDW state. Our results, based on calculations using the Bethe-Salpeter equation and focusing on the Coulomb interaction between holes and electrons, give theoretical support to the hypothesis that strong electron-hole correlations play an important role in 1*T*-$TiSe_2$. The precise interplay between these electronic correlations and lattice dynamics, as well as the role of a possible exciton condensate, have still to be studied in more detail. Persistence above T_c of spectral features reminiscent of the low-temperature ordered phase allows for an interesting comparison with the physics of the pseudogap phase in high-temperature superconductors (HTSC).[16,17] Finally, we also consider the effect of the electron-phonon interaction on the calculated spectra and compare their typical spectral signature to the one of the electron-hole fluctuations, giving further support to the electron-hole fluctuations as the origin of the instability in 1*T*-$TiSe_2$.

II. MODEL

We consider a minimal model for the electronic structure of 1*T*-$TiSe_2$. For simplifying the numerical work, we neglect any dispersion of the bands in the k_z direction. We take into account a single valence band $\varepsilon_a(\vec{k})$ having its maximum at Γ (center of the BZ),

$$\varepsilon_a(\vec{k}) = -\frac{\hbar^2\left(k_x^2 + k_y^2\right)}{2m_a} + \varepsilon_a^0, \tag{1}$$

and three conduction bands $\varepsilon_b^i(\vec{k})$, labeled $i = 1,2,3$, having their minimum at three equivalent M points (on the border of the BZ). Γ is separated from each M by the corresponding spanning vector $\vec{w}_i = \Gamma M$. The dispersion $\varepsilon_b^1(\vec{k})$, for the electron pocket lying along the k_x axis reads (see Ref. 14 for a formula describing the other two pockets)

$$\varepsilon_b^1(\vec{k}) = \frac{\hbar^2(k_x - w_{1x})^2}{2m_{b_x}} + \frac{\hbar^2 k_y^2}{2m_{b_y}} + \varepsilon_b^0. \tag{2}$$

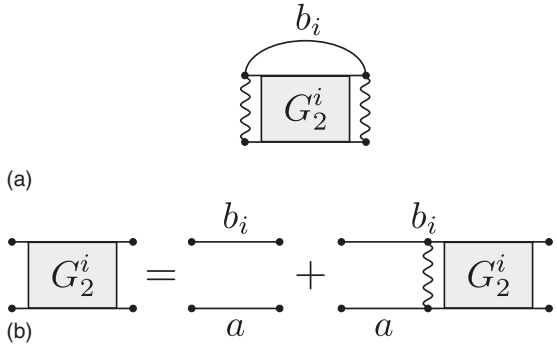

FIG. 1. (a) Diagram for the self-energy of Eq. (9), involving the Coulomb interaction (wavy line). (b) Diagram representation of the Bethe-Salpeter equation (6) for the interacting two-particle Green's function G_2^i, Eq. (4). The lowest order is the product of the valence and the conduction band Green's functions, labeled by a and b_i, respectively.

The corresponding effective masses are m_a and m_{b_x}, m_{b_y}, respectively. The offsets $\varepsilon_a^0 > 0$ and $\varepsilon_b^0 < 0$, with respect to the chemical potential, provide the energy position of the band extrema. In our calculation, we take the chemical potential as the zero of energy. The resulting Fermi surface consists of a symmetric paraboloid in the valence band and an elliptic paraboloid in each of the conduction bands.

The (spinless) Hamiltonian of the model is composed of a one-electron part H_0 for the different bands and a Coulomb interaction part W which contains only the Coulomb interaction between electrons in the valence and in the conduction bands

$$W = \sum_{\vec{q},i} \rho_a(\vec{q}) V(\vec{q}) \rho_{b,i}^\dagger(\vec{q},\vec{w}_i), \tag{3}$$

with the screened Coulomb potential $V(\vec{q}) = e^2/\varepsilon_0(q^2+q_0^2)$, which will be approximated by a local potential, $V(\vec{q}) = V_0$, as discussed below. The partial electron density operators $\rho_a, \rho_{b,i}$, are expressed in the usual way in terms of the fermionic operators $a^\dagger(\vec{k})$ and $b_i^\dagger(\vec{k})$ creating electrons with wave vector $\vec{k}$ in the valence band and in the conduction band i, respectively.

To obtain the self-energies of the valence and the conduction bands, a perturbation calculation is performed in the electron-hole interaction W, following the diagram in Fig. 1(a), similar to the one shown in Ref. 18 [Figs. 2(b) and 2(c), therein]. A basic quantity is the two-particle Green's function G_2^i describing pairs, formed by a hole in the valence band and an electron in the conduction band i. For $i = 1$ it has the form

$$\begin{aligned} &G_2^1(\vec{k}_1,\vec{k}_2,\vec{k}_1',\vec{k}_2',t-t') \\ &\quad = -\langle T a^\dagger(\vec{k}_1,t) b_1(\vec{k}_2+\vec{w}_i,t) b_1^\dagger(\vec{k}_2'+\vec{w}_i,t') a(\vec{k}_1',t')\rangle, \end{aligned} \tag{4}$$

where $\vec{k}_1$ and $\vec{k}_2$ are the wave vectors of the electrons in the valence and the conduction band, respectively. In order to simplify the calculation, the electron wave vectors are transformed into the center-of-mass frame of the electron-hole pair

$$\begin{aligned} \vec{Q} &= \vec{k}_1 - \vec{k}_2 \quad \text{(center-of-mass coordinate)}, \\ p_j &= \frac{m_a k_{2_j} + m_{b_j} k_{1_j}}{m_a + m_{b_j}}, \quad j = x,y \quad \text{(relative coordinate)}. \end{aligned} \tag{5}$$

The same definition holds for $\vec{Q}'$ and $\vec{p}\,'$. Because of the center-of-mass momentum conservation, we have $\vec{Q} = \vec{Q}'$. This two-particle interacting function will be calculated via the Bethe-Salpeter (BS) equation, which is depicted diagrammatically in Fig. 1(b),

$$\begin{aligned} G_2^1(\vec{Q},\vec{p},\vec{p}\,',z_\alpha) &= \delta_{\vec{p},\vec{p}\,'} G_2^{1,(0)}(\vec{Q},\vec{p},z_\alpha) + i\, G_2^{1,(0)}(\vec{Q},\vec{p},z_\alpha) \\ &\quad \times \sum_{\vec{q}} V(\vec{q}) G_2^1(\vec{Q},\vec{p}+\vec{q},\vec{p}\,',z_\alpha). \end{aligned} \tag{6}$$

The noninteracting Green's function $G_2^{1,(0)}$ has the form

$$G_2^{1,(0)}(\vec{Q},\vec{p},z_\alpha) = \frac{\mathcal{N}(\vec{p},\vec{Q})}{z_\alpha - \left[\varepsilon_b^1(\vec{p},\vec{Q}) - \varepsilon_a(\vec{p},\vec{Q})\right]}, \tag{7}$$

with the thermodynamical factor $\mathcal{N}(\vec{p},\vec{Q}) = N_F(\varepsilon_a(\vec{p},\vec{Q})) - N_F(\varepsilon_b(\vec{p},\vec{Q}))$, N_F being the Fermi-Dirac distribution. The $(\vec{p},\vec{Q})$ dependence of the dispersions are a consequence of the transformations (5) for $\varepsilon_a(k_1)$ and $\varepsilon_b^1(\vec{k}_2)$ [see Eqs. (1) and (2)].

The replacement of the screened Coulomb potential by V_0 allows us to integrate out the wave vectors $\vec{p}, \vec{p}\,'$ of the two-particle Green's functions in the BS equation (6), giving rise to the new functions $X_i(\vec{Q},z) = i \sum_{p,p'} G_2^i(\vec{Q},\vec{p},\vec{p}\,',z)$, expressed in terms of $X_i^{(0)}(\vec{Q},z) = i \sum_p G_2^{i,(0)}(\vec{Q},\vec{p},z)$, as follows:

$$X_i(\vec{Q},z) = \frac{X_i^{(0)}(\vec{Q},z)}{1 - V_0 X_i^{(0)}(\vec{Q},z)}. \tag{8}$$

With these ingredients, the self-energy of the valence band is determined by [cf. Fig. 1(a)]

$$\begin{aligned} \sigma_a(\vec{p},z_\alpha) &= V_0^2 \sum_{\vec{Q},i} \int \frac{d\omega}{2\pi} \mathcal{X}_{X_i}(\vec{Q},\omega) \\ &\quad \times \frac{N_B(\omega) + N_F[\varepsilon_{b_i}(\vec{p}+\vec{Q})]}{z_\alpha + \omega - \varepsilon_{b_i}(\vec{p}+\vec{Q})}. \end{aligned} \tag{9}$$

where N_B is the Bose-Einstein distribution. This self-energy directly depends on the dispersion of the conduction band and on the spectral function $\mathcal{X}_{X_i}$ of the integrated two-particle Green's function

$$\mathcal{X}_{X_i}(\vec{Q},\omega) = 2\,\mathrm{Im}[X_i(\vec{Q},\omega+i\eta)], \tag{10}$$

which describes the propagation of an electron-hole pair. In order to simplify the numerical calculations, the unperturbed conduction-band dispersion $\varepsilon_{b_i}(\vec{p})$ is introduced in Eq. (9). A fully self-consistent approach, using a renormalized band dispersion in the calculation of the self-energies, should in principle be done. However, it should not lead to substantially different results, since the parts of the renormalized spectral functions (shown below) which have the largest weight, still more or less follow the bare band dispersion. The calculation of the self-energy of the conduction band i is similar and leads

http://doc.rero.ch

http://doc.rero.ch

to a comparable expression

$$\sigma_{b_i}(\vec{p}+\vec{\omega}_i,z_\alpha) = V_0^2 \sum_{\vec{Q}} \int \frac{d\omega}{2\pi} \mathcal{X}_{X_i}(\vec{Q},\omega) \times \frac{1+N_B(\omega)-N_F[\varepsilon_a(\vec{p}-\vec{Q})]}{z_\alpha-\omega-\varepsilon_a(\vec{p}-\vec{Q})}. \quad (11)$$

Except for the exchange of the band indices, this self-energy differs particularly from the one of the valence band by the thermodynamical factor.

With our definitions, a pair composed of an electron $\varepsilon_{b_i}(\vec{p},\vec{Q})$ and a hole $\varepsilon_a(\vec{p},\vec{Q})$ of center of mass $\vec{Q}=\vec{0}$ has a total momentum w_i. In the following figures, the conduction band is shifted by this vector w_i to have its minimum at Γ. This choice does not change the electron-hole physics but simplifies its visualization.

III. NUMERICAL RESULTS

We now turn to the numerical evaluation (using the CUBA library[19]) of the self-energies of the valence and the conduction bands. Our model band structure, given by Eqs. (1) and (2), is displayed in Fig. 2. Panel (a) shows the dispersion of the valence and of the conduction bands around their extrema and along the ΓM direction. The parameters of these dispersions are chosen as $\varepsilon_a^0 = 0.03$ eV, $\varepsilon_b^0 = -0.04$ eV, $m_a = m_e$, $m_{b_x} = 5.5m_e$, and $m_{b_y} = 0.5m_e$ (m_e is the bare electron mass), giving rise to a band structure similar to the one measured in 1T-$TiSe_2$ and producing a Fermi surface [panel (b)] with four "crossing" points (where the valence and conduction bands cross each other at E_F). They are emphasized by arrows on the Fermi surface displayed in Fig. 2(b). The (orange) circle is the hole pocket from the valence band and the (blue) ellipse is an electron pocket from the conduction band.

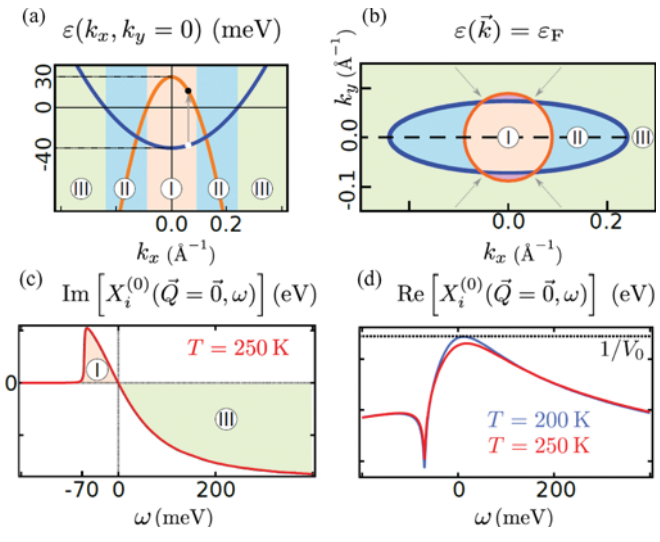

FIG. 2. (Color online) (a) Band structure along k_x for $k_y = 0$ considered in our calculations, with a single valence band at Γ (orange) and one of the three symmetry equivalent conduction bands at M (blue) shifted on this graph to Γ. (b) Corresponding Fermi surface. (c) Imaginary part of $X_i^{(0)}(\vec{Q},\omega)$, the integrated noninteracting two-particle Green's function, at $\vec{Q}=\vec{0}$. Two regimes are distinguished and related to the band structure in graph (b). (d) Real part of $X_i^{(0)}(\vec{Q},\omega)$ (see text).

The spectral function of the integrated two-particle Green's function $X_i(\vec{Q},\omega)$ plays a central role in the self-energies of the valence and conduction bands [see Eqs. (9) and (11)]. We first discuss the case of its noninteracting version, $X_i^{(0)}(\vec{Q},\omega)$. In Fig. 2(c), we show the imaginary part of $X_i^{(0)}(\vec{Q},\omega)$ at $\vec{Q}=\vec{0}$ (and $T = 250$ K), where two domains have been delimited on each side of $\omega = 0$. Nonzero contributions are produced by transitions between the valence and the conduction bands at a certain energy transfer ω [such an excitation is sketched in Fig. 2(a)]. The large (green) feature building up at $\omega > 0$ in Fig. 2(c) is related to transitions away from the band extrema, in the (green) region III of Fig. 2(b) (see Ref. 20 for a similar discussion below T_c.) The (orange) peak extending to energies below $\omega = 0$ are related to transitions near $\vec{k}=\vec{0}$ (region I). In Fig. 2(d), we show the real part of $X_i^{(0)}(\vec{Q},\omega)$ at $\vec{Q}=\vec{0}$ for two different temperatures. From Eq. (8), X_i diverges when $\mathrm{Im}(X_i^{(0)}) \to 0$ and $\mathrm{Re}(X_i^{(0)}) \to 1/V_0$. The first condition is fulfilled at $\omega = 0$ for any temperature, while the second depends on the value of V_0. In order to obtain a divergence at $T = 200$ K, we find $V_0 \approx 0.4$ eV Å^3. Attributing this value to V_0 corresponds to a reasonable replacement of the screened Coulomb interaction by a local potential. Its value can also be obtained by integrating the real-space screened Coulomb potential $V(\vec{r})$ over a sphere of radius $r_\lambda = 1.6$ Å. This distance is slightly larger than the screening length of 1.2 Å, which can be estimated by using the Thomas-Fermi screening theory and the measured plasma frequency in 1T-$TiSe_2$.[21] The fact that these distances are about one half of the nearest-neighbor distance justifies the use of a local potential.

Figure 3 illustrates the divergence of the electron-hole susceptibility $X_i(\vec{Q},\omega)$. In graphs (a) and (b) are shown its imaginary and real parts for different temperatures. The divergence develops as the temperature decreases towards $T = 200$ K. This instability of the electron-hole system takes place at $\vec{Q}=0$ and $\omega = 0$ and it corresponds to the Thouless criterion[18] for the transition, at $T = 200$ K, to a possible exciton condensate. It is characterized by the wave vectors $\vec{w}_i$, since, for $\vec{Q}=0$, the wave vectors of the electron and of the hole in G_2^i in Eq. (4) differ precisely by $\vec{w}_i$. A fully three-dimensional calculation would be based on the minima of the conduction band lying at L, rather than at

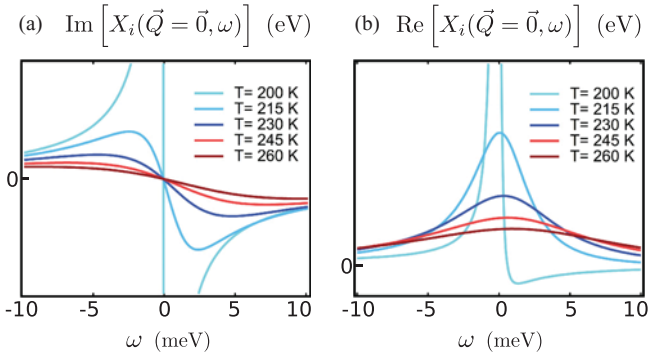

FIG. 3. (Color online) Temperature dependence of the (a) imaginary and (b) real parts of $X_i(\vec{Q}=\vec{0},\omega)$.

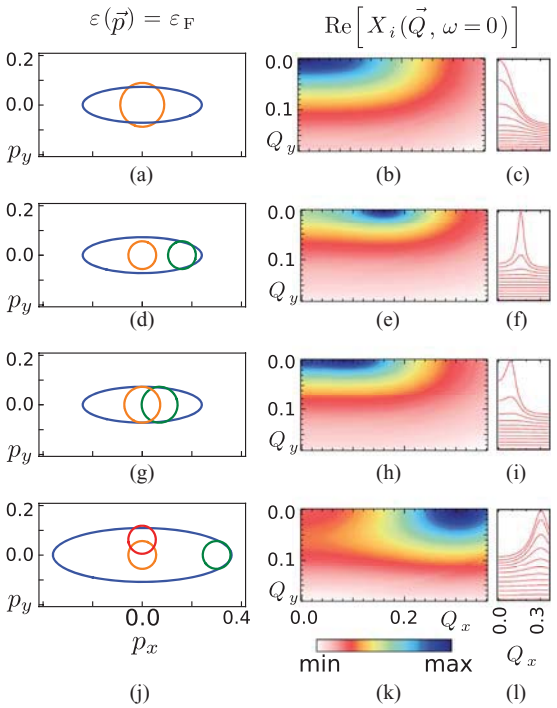

FIG. 4. (Color online) Four different Fermi-surface configurations (first column) are discussed (when the hole pocket is drawn in orange color, it is the configuration for $\vec{Q} = \vec{0}$; in green or red colors, the Fermi pockets are shifted by a center-of-mass wave vector $\vec{Q} \neq 0$). Depending on the situation, the divergence of $\mathrm{Re}[X_i^{(0)}(\vec{Q},\omega = 0)]$ occurs for different $\vec{Q}$ vectors (second column, in false color plots). The third column also displays $\mathrm{Re}[X_i^{(0)}(\vec{Q},\omega = 0)]$ as a function of Q_x for different Q_y from 0.0 (top curve) to 0.18 (bottom curve), in arbitrary units. The wave vectors are given in Å^{-1}.

M. The corresponding wave vectors $\vec{w}_i$ would then exactly correspond to the new periodicity of the electronic charge in the low-temperature CDW phase.[13] Therefore this scenario indeed shows the relevance of electron-hole correlations in the formation of the $(2 \times 2 \times 2)$ CDW of $1T$-$TiSe_2$, which is commensurate, in spite of the absence of a real nesting vector.[22] The nesting between valence and conduction bands, which is often taken as the driving force of a CDW transition, is replaced by the crossing of the corresponding Fermi surfaces at the four points shown in Fig. 2(b). We shall now discuss this issue in more detail before discussing the influence of the electron band self-energies on the spectral function.

In order to understand the influence of the Fermi-surface configuration on the wave vector characterizing the electronic instability, we consider three other Fermi-surface configurations in addition to the one discussed above. Our results are summarized in Fig. 4. For explaining the different behaviors, it is useful to consider Eq. (7) for $G_2^{1,(0)}$, which involves in its denominator the difference between the energies of a valence and of a conduction-band state.

At low temperature the numerator is nonzero essentially only when one of the states is occupied and the other one is empty. For $z = 0$, the denominator in the sum is small when the involved valence- and conduction-band energies are close to the Fermi surface. For our configuration (a) this is the case near the four crossing points for which the center-of-mass momentum Q is zero. Thus the peak in $\mathrm{Re}(X_i^{(0)})$, and the instability of $\mathrm{Re}(X_i)$, occur at $\vec{Q} = 0$. However, in configuration (d), where the effective mass of the valence band is reduced ($m_a = 0.4m_e$), there are no crossing points. The most important contribution to the sum over $\vec{p}$ (appearing in the definition of $X_i^{(0)}$) will come from regions where, for a given $\vec{Q}$, a small difference in the denominator can be maintained on a relatively large segment of Fermi surface in the $\vec{p}$ sum. For configuration (d), this is the case for $Q_x \approx 0.2$ Å^{-1} and Q_y small. Indeed, when the valence-band Fermi surface is shifted by $Q_x \approx 0.2$ Å^{-1} [in green in Fig. 4(d)], it touches the ellipse of the conduction-band Fermi surface. Therefore this configuration corresponds more to the Fermi-surface nesting, well known for Peierls transitions, and the vector, for which the instability occurs, joins the portions of the two Fermi surfaces with a similar curvature. For an intermediate case, a configuration for which the hole pocket diameter is exactly matching the short axis of the elliptical electron pocket [Fig. 4(g)], a nonzero wave vector $\vec{Q} \approx (0.07,0)$ Å^{-1}, is again preferred. Indeed, shifting the hole pocket by this nonzero Q_x (see green circle) leads to a configuration where the nesting between the two Fermi surfaces is more favorable. For configuration (d), one should note that there is no more favorable configuration for a nonzero Q_y at $Q_x = 0$ [see panel (e)]. The reason is that the two Fermi surfaces are too close to each other. In the configuration (j), the conduction-band minimum is shifted to -90 meV such that its Fermi surface is enlarged. In this case [see panel (k)], there is a favorable situation for a finite Q_y (corresponding to the displaced red circle) also, in addition to the (dominant) one occurring along Q_x (green circle). However, the real divergence builds up for $Q_y = 0$ and Q_x around 0.3 Å^{-1}.

It should be noticed that for the Fermi-surface configurations of Figs. 4(d), 4(g) and 4(j), the value of V_0 had to be increased to 0.68, 0.49, and 0.72 eV Å^3, respectively, for keeping the electronic instability at 200 K. It means that these configurations are less susceptible to lead to an electronic instability than the one of Fig. 4(a).

We would also like to note that any interaction potential $V(\vec{r})$, which acts between the valence and conduction bands and can be approximated by a local potential with a sufficient amplitude, and which leads to self-energies having the same form as those of Eqs. (9) and (11) will essentially result in the same phenomenology as described in this article.

IV. SPECTRAL FUNCTION: COMPARISON TO EXPERIMENT

Figures 5(a)–5(f) display the photoemission intensity maps calculated numerically with the self-energies of Eqs. (9) and (11), using the band dispersions shown in Fig. 2(a). Graphs (a) and (b) of Fig. 5 show the results for the valence and the conduction bands. In graphs (c) and (d) are displayed the corresponding energy distribution curves. Around Γ [Fig. 5(a)], for the valence band, two separate bands are clearly distinguished. The top of the valence band (labeled c) is higher above E_F and has a high intensity around its local maximum situated at about 85 meV, vanishing then for larger values of the wave vector. The rest of the band (v) is shifted below E_F,

http://doc.rero.ch

http://doc.rero.ch

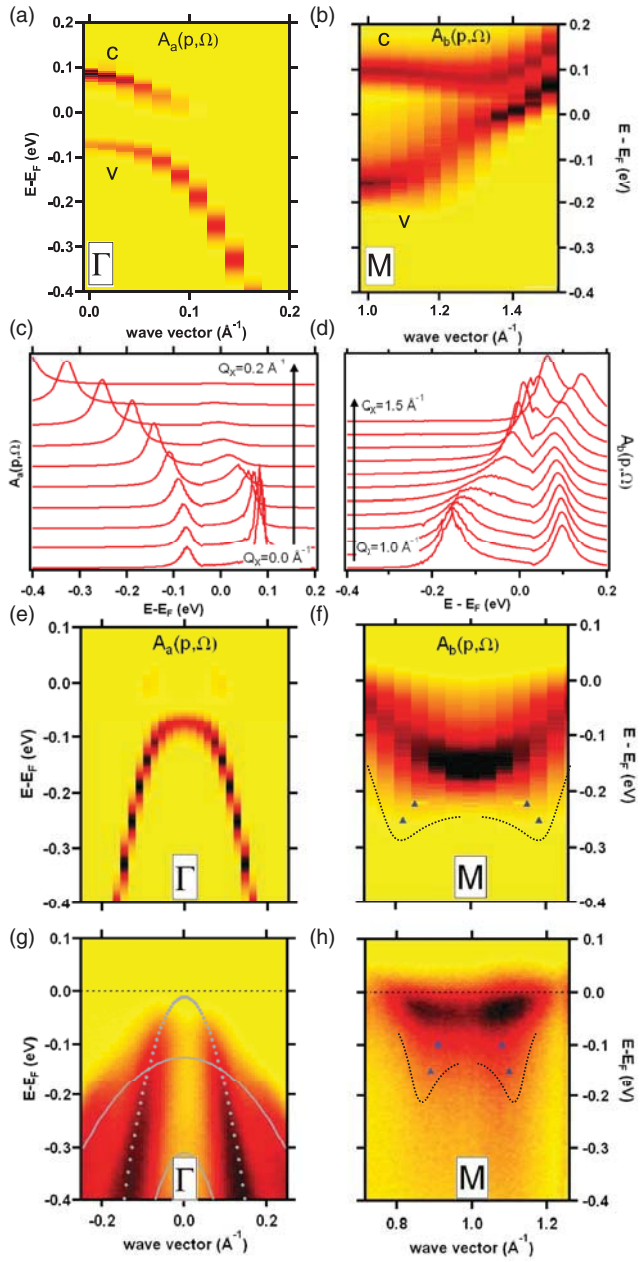

FIG. 5. (Color online) Photoemission intensity maps calculated in the fluctuation regime above T_c (at 250 K) at Γ (a) and at M (b), without considering the Fermi-Dirac cutoff. Graphs (c) and (d) show the corresponding energy distribution curves. In graphs (e) and (f), same as (a) and (b), but symmetrized around the band extremum and cut by a Fermi-Dirac cutoff. Photoemission intensity maps measured at 250 K (g) at Γ and (h) at M in the surface BZ, from Ref. 11. Guides to the eyes (dashed curves and triangles) have been added to emphasize the faint backfolded band in the calculation (f) and in the experiment (h).

at about −70 meV, and its intensity, which is low around its maximum, increases as the wave vector increases. As the peak of the bare band shifts away from E_F, its width increases too. In graph (b), around M, the conduction band is split in two parts, one dispersing mainly above E_F and one below E_F. Above E_F, the band (labeled c) is quite sharp and has a local maximum at 95 meV, while below E_F the band (v) is broader and has a minimum at −155 meV.

In our previous work on the exciton condensate phase,[11] we interpreted our photoemission data on 1T-$TiSe_2$ within the exciton condensate phase model developed at the mean-field level and characterized by an order parameter. Although formally not correct, this approach was also used to simulate the photoemission data above T_c with a nonzero order parameter and with a constant nonzero imaginary self-energy to broaden the delta peaks. In the present calculation, the width of the band, which increases with binding energy, comes naturally from the imaginary part of the self-energy and is due the electron-hole scattering. Comparing experimental data at 250 K (Ref. 11) [Figs. 5(g) and 5(h)] with the calculated data [Figs. 5(e) and 5(f), as Figs. 5(a) and 5(b) but symmetrized around Γ, respectively, M, and cut by a Fermi-Dirac distribution], we observe the following. At Γ, we find good overall agreement with the calculated data. Notice that, in the experiment, three Se 4p valence bands, highlighted by (gray) lines in Fig. 5(g), are observed at Γ, whereas only the topmost one (dashed line) is considered for simplicity in our model (see Ref. 11 for more details). In particular, the opening of a gap, the shifting of the valence band below E_F, and the loss of intensity at its maximum are reproduced here, as in the mean-field approach.[11]

At M, the situation is different. In the mean-field approach, the artificial use of a small nonzero order parameter above T_c was leading to the appearance of a narrow backfolded valence band below the conduction band[11] with a width given by the constant nonzero imaginary self-energy. Now, in Fig. 5(f), the electron-hole fluctuations produce a strong broadening of the conduction band, together with low intensity tails at higher binding energy, which anticipate the presence of the backfolded valence band below T_c. Despite their lower intensity in the calculation, possibly due to some higher-order effects not captured in the present analytical treatment, this is in better agreement with the experimental photoemission data taken at M and at 250 K, shown in Fig. 5(h), where below the surprisingly broad conduction band residual intensity appears. The residual higher intensity below the conduction band, together with the shift of the valence band at Γ, is thus a clear spectral signature of the fluctuation regime above T_c. These findings are also interesting with respect to the HTSC community, as they show that spectral features typical of the low-temperature ordered phase are surviving above the critical temperature, giving rise to diffuse intensity as a consequence of phase fluctuations.

Finally, it appears that the calculated spectra produce bands at too high binding energies compared to the experiment. This is certainly due to the fact that the chemical potential was left constant in these calculations. Because of the redistribution of spectral weight in the fluctuation regime, the chemical potential has to shift downwards to compensate for the numerous new states occupied in the (three) broad conduction bands at M, despite the small loss of occupied states at the top of the valence band at Γ. Thus the good qualitative agreement with the experimental data gives support for the relevance of strong electron-hole correlations. They get stronger when T approaches the temperature of the transition to the CDW phase in a symmetry-breaking superstructure. Their influence on the

http://doc.rero.ch

structural transformation and the possible occurrence of an excitonic instability in $1T$-$TiSe_2$, which has allowed for an understanding of the electronic spectral functions in the CDW phase, has still to be clarified in more detail.

V. ALTERNATIVE EXPLANATION: ELECTRON-PHONON INTERACTION

As an alternative scenario, we now evaluate the influence of the electron-phonon interaction on the electronic spectral functions. The coupling between the electrons and the lattice has certainly to play an important role in the CDW instability in $1T$-$TiSe_2$, given the fact that the formation of the CDW is accompanied by a periodic lattice deformation. Such a scenario has been already invoked for $1T$-$TiSe_2$ in the framework of the (band) Jahn-Teller distortion[23–25] or also in addition to the excitonic mechanism.[8]

In addition to the one-electron Hamiltonian containing the electronic dispersions (1) and (2), we consider the electron-phonon interaction term

$$H_{\text{el-ph}} = \sum_{\vec{k}\vec{q}} g_{ba}(\vec{k},\vec{q}) b_i^{\dagger}(\vec{k}) a(\vec{k}-\vec{q}) Q(\vec{q}) + \text{H.c.} \qquad (12)$$

between the valence- and conduction-band electrons. Here Q represents the normal coordinate of the particular phonon coupling these electrons together. The electron-phonon coupling function $g_{ba}(\vec{k},\vec{q})$ will then be approximated by a constant in reciprocal space, i.e., a local interaction in real space, in analogy to what has been done for the Coulomb interaction previously.

Performing a perturbation calculation in $H_{\text{el-ph}}$ leads to a standard formula[26] for the electron self-energy of the valence band due to the coupling of the electrons to the L_1-phonon mode

$$\sigma_a(\vec{p},z_\alpha) = |g_{ba}|^2 \sum_{\vec{K},i} \int \frac{d\omega}{2\pi} \mathcal{X}_{ph}(\vec{K},\omega) \times \frac{N_B(\omega) + N_F[\varepsilon_{b_i}(\vec{p}+\vec{K})]}{z_\alpha + \omega - \varepsilon_{b_i}(\vec{p}+\vec{K})}. \qquad (13)$$

$\vec{K}$ is the phonon wave vector relative to the corresponding L point in reciprocal space. This formula is very similar that of Eq. (9), except that there is a different coupling constant and the spectral function of the electron-hole correlator is replaced by the phonon spectral function $\mathcal{X}_{ph}$, for which we choose a form with a finite line width ϵ,

$$\mathcal{X}_{ph}(\vec{K},\omega) = \frac{\pi}{2\omega(\vec{K},T)} \left[\frac{1}{\epsilon\sqrt{2\pi}} \mathrm{e}^{-[\omega-\omega(\vec{K},T)]^2/2\epsilon^2} - \frac{1}{\epsilon\sqrt{2\pi}} e^{-[\omega+\omega(\vec{K},T)]^2/2\epsilon^2} \right].$$

A self-energy similar to Eq. (13) is derived for the conduction band.

For performing numerical evaluations, we have to use a large value for the electron-phonon coupling constant g_{ba}, namely, $g_{ba} = 2 \times 10^{12}$ eV Å^{-1} kg$^{-1/2}$ (which is about twice larger than what is found using the tight-binding formula of Ref. 27) in order to emphasize the characteristic features of the electron-phonon interaction in the electron spectral function. Furthermore, based on the experimental works of Refs. 28 and 29, we approximate the (transverse optic) L_1-phonon dispersion $\omega(K,T)$, which is softening at T_c, with the formula[30]

$$\omega(\vec{K},T) = \sqrt{[a(T-T_c)]^2 + (bK)^2},$$

for $a = 0.000\,05$ eV/K and $b = 0.04$ eV Å (and $T_c = 200$ K). We also use a phonon linewidth of $\epsilon = 3$ meV.[29]

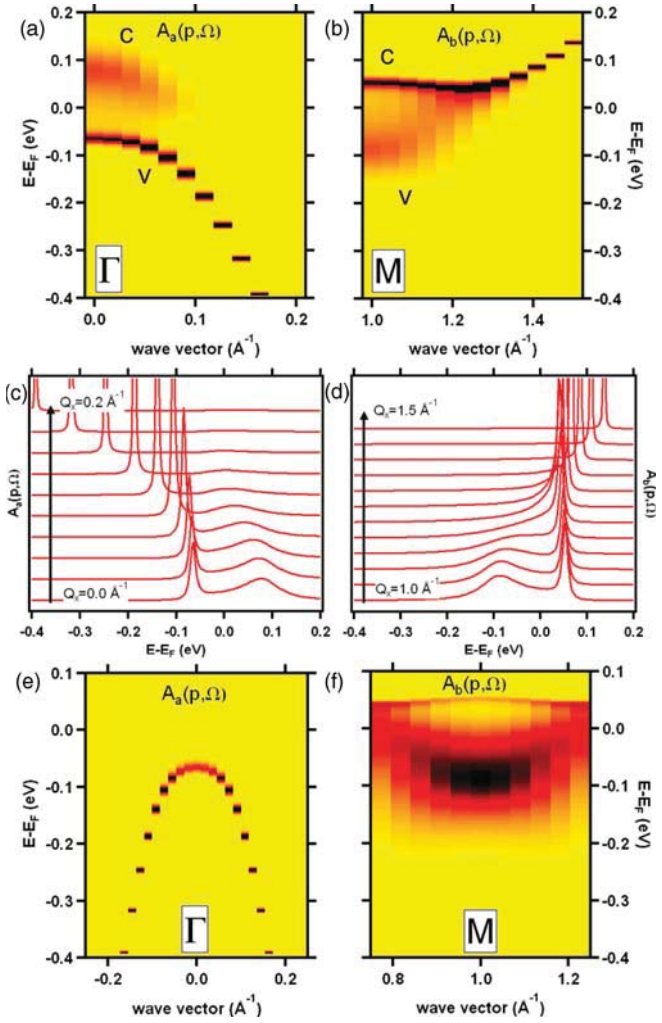

FIG. 6. (Color online) Photoemission intensity maps calculated in the fluctuation regime due to the electron-phonon interaction above T_c (at 220 K) at Γ (a) and at M (b), without considering the Fermi-Dirac cutoff. Graphs (c) and (d) show the corresponding energy distribution curves. In graphs (e) and (f), same as (a) and (b), but symmetrized around the band extremum and cut by a Fermi-Dirac cutoff.

Figures 6(a)–6(f) display the photoemission intensity maps calculated numerically at 220 K with the self-energy of Eq. (13) and the corresponding one for the conduction band, using the band dispersions shown in Fig. 2(a). At first sight, the effect of the electron-phonon interaction on the model band structure is quite similar to what has been observed in Fig. 5 due to the electron-hole fluctuations. At Γ [Fig. 6(a)], a gap opens at E_F, shifting the band (v) to higher binding energies, while a backfolded band (c) appears above E_F. At M [Fig. 6(b)], the band (c) is shifted above E_F and a backfolded band (v) emerges below E_F. However, having a closer look,

especially at the energy distribution curves of Figs. 6(c) and 6(d), one sees characteristic differences. In the case of the electron-phonon interaction, the original bands are extremely sharp [band (v) in Fig. 6(a) and band (c) in Fig. 6(b)], being the quasiparticle peak, while the backfolded bands [band (c) in Fig. 6(a) and band (v) in Fig. 6(b)] are very broad, being the incoherent peak. These are typical spectral signatures of the electron-phonon interaction in metals.[31,32] In our case, it affects the spectra on an energy scale of about 50–100 meV around E_F due to the phonon dispersion combined with the backfolded band dispersion [see Eq. (13)].

We now focus on the photoemission intensity maps cut by a Fermi-Dirac cutoff. Comparing the situation at Γ for the electron-hole fluctuations [Fig. 5(e)] and the electron-phonon interaction [Fig. 6(e)], one sees similar spectra. However, the valence band is broader (in energy) in the case of electron-hole fluctuations, over the full energy range of the spectrum, in agreement with the experiment [Fig. 5(g)]. At M, the electron-phonon interaction causes in both cases [Figs. 5(f) and 6(f)] a broad backfolded valence band with tails extending to higher binding energies [anticipating the full backfolded valence band at $T < T_c$ (Ref. 15)]. However, in the case of the electron-phonon interaction [Fig. 6(f)], the intense quasiparticle peak above E_F still resists to the Fermi-Dirac cutoff, leaving a sharp peak above E_F in the photoemission intensity map, in disagreement with the experiment [Fig. 5(h)].

To sum up, the absence of any sharp quasiparticle peak in the measured spectra above T_c, a quasiparticle peak which is typical of the effect of the electron-phonon interaction in the spectral function, as well as the broad valence band (at Γ) observed up to high binding energies, typical of the scattering to electron-hole pairs, give strong support to the electron-hole fluctuations as the origin of the CDW instability in $1T$-$TiSe_2$.

VI. CONCLUSION

In conclusion, we have studied the fluctuation regime above the critical temperature T_c of the formation of the charge-density-wave phase of $1T$-$TiSe_2$. The Bethe-Salpeter equation has been used in order to handle the electron-hole fluctuations and to determine the influence of the latter on the electronic self-energies. We identified various spectral features characteristic of this regime. They show the increasing strength of electron-hole fluctuations going towards an instability leading to the low-temperature charge-density phase. The wave vectors at which the instability occurs correspond to the $(2 \times 2 \times 2)$ structure of the CDW phase. The calculated photoemission intensity maps compare well with photoemission data obtained for $1T$-$TiSe_2$ at $T = 250$ K, providing us with a better understanding of the dynamics of the electron-hole correlations which can lead to the appearance of an exciton condensate phase below T_c in this system, the scenario which we have used before in order to interpret the low-temperature features of the spectra. Finally, we have also considered the effect of the electron-phonon interaction on the calculated spectra to discriminate what mechanism is responsible for the instability in $1T$-$TiSe_2$. The absence of the typical spectral signatures of the electron-phonon interaction in the measured spectra gives further support to the electron-hole fluctuation scenario.

ACKNOWLEDGMENTS

We acknowledge fruitful discussions with H. Fehske and F. X. Bronold. C.M. also thanks Christophe Berthod for his enlightening on Green's functions. This project was supported by the Fonds National Suisse pour la Recherche Scientifique through Div. II and the Swiss National Center of Competence in Research MaNEP.

*philipp.aebi@unifr.ch

[1] L. V. Keldysh and Y. V. Kopaev, Sov. Phys. - Solid State **6**, 2219 (1965); D. Jérome, T. M. Rice, and W. Kohn, Phys. Rev. **158**, 462 (1967).

[2] Y. Wakisaka, T. Sudayama, K. Takubo, T. Mizokawa, M. Arita, H. Namatame, M. Taniguchi, N. Katayama, M. Nohara, and H. Takagi, Phys. Rev. Lett. **103**, 026402 (2009).

[3] B. Bucher, P. Steiner, and P. Wachter, Phys. Rev. Lett. **67**, 2717 (1991); P. Wachter, B. Bucher, and J. Malar, Phys. Rev. B **69**, 094502 (2004).

[4] P. M. R. Brydon and C. Timm, Phys. Rev. B **80**, 174401 (2009).

[5] N. B. Brandt and S. M. Chudinov, J. Low. Temp. Phys. **8**, 339 (1972).

[6] Y. Wang and M. Y. Chou, Phys. Rev. Lett. **71**, 1226 (1993).

[7] B. Zenker, D. Ihle, F. X. Bronold, and H. Fehske, Phys. Rev. B **83**, 235123 (2011); V. N. Phan, H. Fehske, and K. W. Becker, Europhys. Lett. **95**, 17006 (2011).

[8] J. van Wezel, P. Nahai-Williamson, and S. S. Saxena, Phys. Rev. B **81**, 165109 (2010); **83**, 024502 (2011).

[9] J. A. Wilson and S. Mahajan, Commun. Phys. (London) **2**, 23 (1977).

[10] J. A. Wilson, Phys. Status Solidi B **86**, 11 (1978).

[11] H. Cercellier, C. Monney, F. Clerc, C. Battaglia, L. Despont, M. G. Garnier, H. Beck, P. Aebi, L. Patthey, H. Berger, and L. Forrò, Phys. Rev. Lett. **99**, 146403 (2007).

[12] C. M. Fang, R. A. de Groot, and C. Haas, Phys. Rev. B **56**, 4455 (1997).

[13] F. J. Di Salvo *et al.*, Phys. Rev. B **14**, 4321 (1976).

[14] C. Monney, H. Cercellier, F. Clerc, C. Battaglia, E. F. Schwier, C. Didiot, M. G. Garnier, H. Beck, P. Aebi, H. Berger, L. Forrò, and L. Patthey, Phys. Rev. B **79**, 045116 (2009).

[15] C. Monney, E. F. Schwier, M. G. Garnier, N. Mariotti, C. Didiot, H. Beck, P. Aebi, H. Cercellier, J. Marcus, C. Battaglia, H. Berger, and A. N. Titov, Phys. Rev. B **81**, 155104 (2010).

[16] M. R. Norman, D. Pines, and C. Kallin, Adv. Phys. **54**, 715 (2005).

[17] H.-B. Yang, J. D. Rameau, P. D. Johnson, T. Valla, A. Tsvelik, and G. D. Gu, Nature (London) **456**, 77 (2008).

[18] F. X. Bronold and H. Fehske, Phys. Rev. B **74**, 165107 (2006).

[19] T. Hahn, Comput. Phys. Commun. **168**, 78 (2005).

[20] J. Zittartz, Phys. Rev. **162**, 752 (1967).

[21] G. Li, W. Z. Hu, D. Qian, D. Hsieh, M. Z. Hasan, E. Morosan, R. J. Cava, and N. L. Wang, Phys. Rev. Lett. **99**, 027404 (2007).

http://doc.rero.ch

[22] J. van Wezel, P. Nahai-Williamson, and S. S. Saxena, Eur. Phys. Lett. **89**, 47004 (2010).
[23] H. P. Hughes, J. Phys. C **10**, L319 (1977).
[24] N. Suzuki, A. Yamamoto, and K. Motizuki, J. Phys. Soc. Jpn. **54**, 4668 (1985); Y. Yoshida and K. Motizuki, *ibid*. **49**, 898 (1980).
[25] M. Calandra and F. Mauri, Phys. Rev. Lett. **106**, 196406 (2011).
[26] G. D. Mahan, *Many-Particle Physics* (Plenum, New York, 1981).
[27] C. Monney, C. Battaglia, H. Cercellier, P. Aebi, and H. Beck, Phys. Rev. Lett. **106**, 106404 (2011).
[28] M. Holt, P. Zschack, H. Hong, M. Y. Chou, and T.-C. Chiang, Phys. Rev. Lett. **86**, 3799 (2001).
[29] F. Weber, S. Rosenkranz, J.-P. Castellan, R. Osborn, G. Karapetrov, R. Hott, R. Heid, K.-P. Bohnen, and A. Alatas, Phys. Rev. Lett. **107**, 266401 (2011).
[30] Although the L_1^- phonon is found experimentally to soften at L, we use in our calculations a phonon dispersion softening at M. Indeed, in this paper the k_z dispersion is neglected, so that L is assimilated here to M in our two-dimensional Brillouin zone.
[31] M. Hengsberger, D. Purdie, P. Segovia, M. Garnier, and Y. Baer, Phys. Rev. Lett. **83**, 592 (1999).
[32] T. Cuk, D. H. Lu, X. J. Zhou, Z.-X. Shen, T. P. Devereaux, and N. Nagaosa, Phys. Status Solidi B **242**, 11 (2005).

http://doc.rero.ch